Engineering with Computers
https://doi.org/10.1007/s00366-021-01503-7

ORIGINAL ARTICLE

Strong-form meshfree collocation method for non-equilibrium solidification of multi-component alloy

Peter Schaefferkoetter[1] · **John G. Michopoulos**[2] · **Jeong-Hoon Song**[1]

Received: 29 June 2021 / Accepted: 21 August 2021

Abstract
This work presents a strong form meshfree collocation method for a multi-phase field model with finite dissipation effects due to rapid solidification. We use the collocation method to simulate and study solidification of a low concentration (0.2 at% Sn) Al–Sn binary alloy system under periodic boundary conditions to address non-equilibrium solidification. Numerical implementation takes place through spatial discretization of the governing equations with the collocation method followed by application of the Crank–Nicolson method to integrate through time. Analysis begins with a benchmark, a simple two-grain case with symmetry in domain size, grain positioning, and boundary conditions to study the behavior of the field equations and key terms embedded within. This occurs by studying field and embedded term values along the axis of symmetry. Solidification analysis is then extended for 10 and 20 grains where upon full solidification, the regions with the highest overall concentrations exist within grain boundary region consisting for four or more adjacent grains. An analysis of alloy solidification over a substrate demonstrates epitaxial nucleation and growth.

Keywords Multi-component alloy · Non-equilibrium · Solidification · Phase field model · Strong form · Meshfree collocation

1 Introduction

Solidification is a phase transformation process of a liquid to solid that mainly determines crystallographic characteristics of polycrystalline materials. A polycrystalline microstructure of metallic materials consists of multiple grains with different crystallographic orientations which are separated by grain boundaries. Such a grain structure evolves during the solidification process via grain growth. The importance of polycrystalline microstructures in being associated with many of the macroscopic mechanical properties has been well known [1–3].

Rapid solidification processes occur at extremely small timescales, leaving the material little to no opportunity to adapt the extreme thermal gradients imposed upon it. In addition, the solidification front travels so quickly leaving insufficient time for the material to relax towards equilibrium, and gradients in composition ahead of the front cannot fully develop or evolve.

Both sharp interface [4–7] and diffusive interface, i.e. phase field [8–10] methods have been used to predict various non-equilibrium thermodynamic models capable of addressing rapid solidification and related phenomena. The phase field model is a versatile tool that can track the evolution of complex interface geometry. The models have been originally developed for solidification of pure materials [11–13], and then extended to alloy system. For example, Wheeler et al. developed a phase field model for a binary alloy [14], and further extended to study solute trapping [15, 16]. Phase field models for solidification of eutectic alloys are also available in the literature [17–19] including the isothermal growth of an ideal solution of a binary alloy with dendritic growth patterns [20]. More recently, a multiscale coupled finite element and phase field framework for the prediction of stressed grain growth has been developed [21].

In this work, we explore the multi-phase field model of Steinbach et al. [8] with a recently developed strong form-based collocation method [22–24] to consider the rapid solidification of multi-component alloy system. In this multi-phase field model, the energy functional F comprised

✉ Jeong-Hoon Song
jh.song@colorado.edu

[1] Department of Civil, Environmental and Architectural Engineering, University of Colorado, Boulder, CO 80309, USA

[2] Computational Multiphysics Systems Laboratory, Naval Research Laboratory, Washington, DC 20375, USA

Published online: 08 September 2021

of interfacial f^{int} and chemical f^{chem} energy densities. The alloy concentration field c is split into phase concentrations c_α for each phase α; note that c_α is related to c through the weighted sum $c_\alpha\phi_\alpha$ by $c = \sum_{\alpha=1}^{N} c_\alpha\phi_\alpha$ where ϕ_α is the phase field for α. The Gibbs free energy, ϕ_α, c_α, and the constraint $c - \sum_{\alpha=1}^{N} c_\alpha\phi_\alpha = 0$ are embedded within F through f^{int} and f^{chem}. The first variation δF with respect to $\delta\phi_\alpha$ and δc_α produces field equations describing phase $\dot{\phi}_\alpha$ and concentration $\dot{c}_\alpha$ kinetics within the region of active phase change where the latter is scaled by a kinetic permeability coefficient, P. Finally, diffusion terms dependent on the concentration gradient ∇c_α through a coefficient D are added to $\dot{c}_\alpha$. This model, initially applicable to binary solutions, has been extended to the multi-component and multi-phase case [9] where the mixture rule is applied to each solute, i.e. $c^i = \sum_{\alpha=1}^{N} c_\alpha^i\phi_\alpha$.

A strong form based meshfree collocation [22–24] and Crank-Nicholson methods are used to spatially discretize and temporally integrate the multi-phase field evolution equations. The collocation method employs a Taylor expansion and generalized moving least-squares approach to compute discrete differential operators. Application of the computed differential operators to the partial differential equations of interest is a straight forward process. The method has been applied to various physics and engineering based problems, to include a generalized formalism for strong and weak discontinuities [23–25] and moving interface problems [26], polycrystalline solidification with diffusive interface approach [27, 28], inelastic material [29], ocean circulation [30], and frictional contact [31] problems.

In Sect. 2, we provide a description of the meshfree collocation method and its key components. This includes using a Taylor polynomial to approximate a smooth field and its derivative with subsequent conversion to discrete form through the method weighted residuals to yield a set of discrete derivative operators. Section 2 continues with a description of the governing equations, its spatial discretization. Section 3 presents a review of the Crank–Nicolson integration algorithm and summarizes the overall computational procedure used in this study. Section 4 contains numerical studies for alloy solidification for two-grain, ten-grain, and 20-grain cases where the latter considers solidification over a substrate. Conclusions are presented in Sect. 5.

2 The strong form based meshfree collocation method

2.1 Meshfree collocation approximation

We provide a brief overview of the meshfree collocation method adopted in this study; details can be found in the literature [22–24]. The method employs a Taylor series expansion and moving least-square approximation to develop higher-order numerical differential operators. Suppose within a real n-dimensional domain, $\Omega \in \mathbb{R}^n$, there exist a smooth field $u(\mathbf{x})$ differentiable up to order m. The m^{th}-order Taylor polynomial of the field $u(\mathbf{x})$ at the local point $\bar{\mathbf{x}}$ is given by

$$u(\mathbf{x};\bar{\mathbf{x}}) = \sum_{|\boldsymbol{\alpha}|\le m} \frac{(\mathbf{x}-\bar{\mathbf{x}})^{\boldsymbol{\alpha}}}{\boldsymbol{\alpha}!} D_{\mathbf{x}}^{\boldsymbol{\alpha}} u(\bar{\mathbf{x}}) = \mathbf{p}_m^{\top}(\mathbf{x};\bar{\mathbf{x}})\mathbf{a}(\bar{\mathbf{x}}) \tag{1}$$

where

$$D_{\mathbf{x}}^{\boldsymbol{\alpha}} f(\mathbf{x}) = \frac{\partial^{|\boldsymbol{\alpha}|} f(\mathbf{x})}{\partial x_1^{\alpha_1}\partial x_2^{\alpha_2}\dots\partial x_n^{\alpha_n}}. \tag{2}$$

Note that $D_{\mathbf{x}}^{\boldsymbol{\alpha}} f(\mathbf{x})$ corresponds to the $\boldsymbol{\alpha}^{\text{th}}$ derivative of $u(\mathbf{x})$, $\boldsymbol{\alpha} = (\alpha_1, \dots, \alpha_n)$ is restricted to the set of n-tuple of non-negative integers, $|\boldsymbol{\alpha}|$ is the sum of all components of $\boldsymbol{\alpha}$ i.e. $|\boldsymbol{\alpha}| \equiv \sum_{i=1}^{n} \alpha_i$, and $\boldsymbol{\alpha}!$ is the factorial of $\boldsymbol{\alpha}$ which is given by $\boldsymbol{\alpha}! = \alpha_1!\dots\alpha_n!$. The Taylor polynomial in Eq. (1) is further decomposed into a vector $\mathbf{p}_m^{\top}(\mathbf{x};\bar{\mathbf{x}})$ and its associated derivative coefficient vector $\mathbf{a}(\bar{\mathbf{x}})$ computed at the local center $\bar{\mathbf{x}}$. The polynomial vector takes the form:

$$\mathbf{p}_m^{\top}(\mathbf{x};\bar{\mathbf{x}}) = \left[\frac{(\mathbf{x}-\bar{\mathbf{x}})^{\boldsymbol{\alpha}_1}}{\boldsymbol{\alpha}_1!}, \dots, \frac{(\mathbf{x}-\bar{\mathbf{x}})^{\boldsymbol{\alpha}_L}}{\boldsymbol{\alpha}_L!}\right] \tag{3}$$

where $L = (n+m)!/n!m!$ is the number of components for the polynomial vector $\mathbf{p}_m$. Here, $(\mathbf{x}-\bar{\mathbf{x}})^{\boldsymbol{\alpha}_i}$ is the $\boldsymbol{\alpha}_i^{\text{th}}$-power of $\mathbf{x}-\bar{\mathbf{x}}$ defined by $(\mathbf{x}-\bar{\mathbf{x}})^{\boldsymbol{\alpha}_i} = (x_1-\bar{x}_1)^{\alpha_{1i}}(x_2-\bar{x}_2)^{\alpha_{2i}}\dots(x_n-\bar{x}_n)^{\alpha_{ni}}$. The derivative coefficient vector $\mathbf{a}^{\top}(\bar{\mathbf{x}})$ includes all of the derivatives for $u(\bar{\mathbf{x}})$ at the local center up to the $\boldsymbol{\alpha}_L^{\text{th}}$-order and is defined as:

$$\mathbf{a}^{\top}(\bar{\mathbf{x}}) = \left[D_{\mathbf{x}}^{\boldsymbol{\alpha}_1} u(\bar{\mathbf{x}}), \dots, D_{\mathbf{x}}^{\boldsymbol{\alpha}_L} u(\bar{\mathbf{x}})\right]. \tag{4}$$

The generalized moving least-square approximation occurs by minimizing the weighted functional $\mathbf{J}$ with respect to $\mathbf{a}(\bar{\mathbf{x}})$. It is a weighted 2-norm, summed over N neighbors, which provides a measure of distance between the smooth field $u(\mathbf{x})$ and discrete values u_I at the point $\mathbf{x}_I$. The weighting function w is dependent on the distance between the local center $\bar{\mathbf{x}}$ and its neighbor $\mathbf{x}_I$, normalized by a dilatation parameter $\boldsymbol{\rho}$; note that the weighting function w assumes the role determining the neighborhood size and the degree of influence each neighbor has on the local center. In other words,

$$\mathbf{J} = \sum_{I=1}^{N} w\left(\frac{\mathbf{x}_I - \bar{\mathbf{x}}}{\rho_{\bar{\mathbf{x}}}}\right)[\mathbf{p}^{\top}(\mathbf{x}_I)\mathbf{a}(\bar{\mathbf{x}}) - u_I]^2 \tag{5}$$

minimization of $\mathbf{J}$ yields

$$\mathbf{a}(\bar{\mathbf{x}}) = \mathbf{M}^{-1}(\bar{\mathbf{x}})\mathbf{B}(\bar{\mathbf{x}})\mathbf{u}^{\top} \tag{6}$$

where

$$\mathbf{M}(\bar{\mathbf{x}}) = \sum_{I=1}^{N} w\left(\frac{\mathbf{x}_I - \bar{\mathbf{x}}}{\rho_{\bar{\mathbf{x}}}}\right)\mathbf{p}_m(\mathbf{x}_I;\bar{\mathbf{x}})\mathbf{p}_m^{\top}(\mathbf{x}_I;\bar{\mathbf{x}}), \tag{7}$$

$$\mathbf{B}(\bar{\mathbf{x}}) = \left[w\left(\tfrac{\mathbf{x}_1-\bar{\mathbf{x}}}{\rho_{\bar{\mathbf{x}}}}\right)\mathbf{p}_m(\mathbf{x}_1;\bar{\mathbf{x}}),\ \ldots,\ w\left(\tfrac{\mathbf{x}_N-\bar{\mathbf{x}}}{\rho_{\bar{\mathbf{x}}}}\right)\mathbf{p}_m(\mathbf{x}_N;\bar{\mathbf{x}})\right]. \tag{8}$$

Recall that $\mathbf{a}(\bar{\mathbf{x}})$ is the collection of derivative coefficients of $\mathbf{D}_{\mathbf{x}}^{\boldsymbol{\alpha}}u(\mathbf{x})$ and consider an application of Eq. (6) to every point in the domain and its boundary, i.e. $\mathbf{x} \in \Omega \cup \partial\Omega$ to yield a relationship between differential operator and its interpolation function

$$\mathbf{D}_{\mathbf{x}}^{\boldsymbol{\alpha}}u(\mathbf{x}) = \sum_{I=1}^{N} \boldsymbol{\Phi}_I^{\boldsymbol{\alpha}}(\mathbf{x})u_I. \tag{9}$$

In matrix form, Eq. (9) can be expressed as

$$\mathbf{a}(\mathbf{x}) = \begin{pmatrix} \mathbf{D}_{\mathbf{x}}^{\boldsymbol{\alpha}_1}u(\mathbf{x}) \\ \mathbf{D}_{\mathbf{x}}^{\boldsymbol{\alpha}_2}u(\mathbf{x}) \\ \vdots \\ \mathbf{D}_{\mathbf{x}}^{\boldsymbol{\alpha}_L}u(\mathbf{x}) \end{pmatrix} = \begin{pmatrix} \boldsymbol{\Phi}_1^{\boldsymbol{\alpha}_1}(\mathbf{x}) & \boldsymbol{\Phi}_2^{\boldsymbol{\alpha}_1}(\mathbf{x}) & \cdots & \boldsymbol{\Phi}_N^{\boldsymbol{\alpha}_1}(\mathbf{x}) \\ \boldsymbol{\Phi}_1^{\boldsymbol{\alpha}_2}(\mathbf{x}) & \boldsymbol{\Phi}_2^{\boldsymbol{\alpha}_2}(\mathbf{x}) & \cdots & \boldsymbol{\Phi}_N^{\boldsymbol{\alpha}_2}(\mathbf{x}) \\ \vdots & \vdots & \ddots & \vdots \\ \boldsymbol{\Phi}_1^{\boldsymbol{\alpha}_L}(\mathbf{x}) & \boldsymbol{\Phi}_2^{\boldsymbol{\alpha}_L}(\mathbf{x}) & \cdots & \boldsymbol{\Phi}_N^{\boldsymbol{\alpha}_L}(\mathbf{x}) \end{pmatrix} \begin{pmatrix} u_1 \\ u_2 \\ \vdots \\ u_N \end{pmatrix} \tag{10}$$

where $\boldsymbol{\alpha}_i$'s are a n-tuple of non-negative integers; for the two dimensional case, $\boldsymbol{\alpha}_1 = (0,0)$, $\boldsymbol{\alpha}_2 = (1,0)$, $\boldsymbol{\alpha}_3 = (0,1)$, …, $\boldsymbol{\alpha}_L = (0,m)$ for the mth order polynomial vector $\mathbf{p}_m$. Here, $\boldsymbol{\Phi}_I^{\boldsymbol{\alpha}}(\mathbf{x})$ is the $\boldsymbol{\alpha}^{\text{th}}$ derivative of the shape function at node I defined as

$$\boldsymbol{\Phi}_I^{\boldsymbol{\alpha}}(\mathbf{x}) = \mathbf{e}_{\boldsymbol{\alpha}}^{\top}\mathbf{M}^{-1}(\mathbf{x})\mathbf{p}(\mathbf{x}_I;\mathbf{x})w\left(\frac{\mathbf{x}_I - \mathbf{x}}{\rho_{\mathbf{x}}}\right) \tag{11}$$

where $\mathbf{e}_{\alpha}^{\top} = [e_0, \ldots, e_m]$ with its component defined as

$$e_k = \begin{cases} 1 & \text{if } k = \alpha \\ 0 & \text{otherwise} \end{cases} \tag{12}$$

for $k = 0, \ldots, m$.

For an application involving a 2nd-order polynomial in $\mathbb{R}^2$, i.e. $m = 2$ and $n = 2$, the Taylor polynomial (1) approximating the field $u(\mathbf{x})$ centered at a point $\bar{\mathbf{x}} = [\bar{x}_1, \bar{x}_2] \in \Omega$ can be written as

$$\begin{aligned} u(\mathbf{x}) = \ & u(\bar{\mathbf{x}}) + D_{\mathbf{x}}^{(1,0)}u(\bar{\mathbf{x}})(x_1 - \bar{x}_1) + D_{\mathbf{x}}^{(0,1)}u(\bar{\mathbf{x}})(x_2 - \bar{x}_2) \\ & + D_{\mathbf{x}}^{(2,0)}u(\bar{\mathbf{x}})\frac{(x_1 - \bar{x}_1)^2}{2!} + D_{\mathbf{x}}^{(1,1)}u(\bar{\mathbf{x}})(x_1 - \bar{x}_1)(x_2 - \bar{x}_2) \\ & + D_{\mathbf{x}}^{(0,2)}u(\bar{\mathbf{x}})\frac{(x_2 - \bar{x}_2)^2}{2!} \end{aligned} \tag{13}$$

where the polynomial vector takes the form

$$\begin{aligned} & \mathbf{p}_2^{\top}(\mathbf{x};\bar{\mathbf{x}}) \\ & = \left[1 \ (x_1 - \bar{x}_1) \ (x_2 - \bar{x}_2) \ \tfrac{(x_1-\bar{x}_1)^2}{2!} \ (x_1 - \bar{x}_1)(x_2 - \bar{x}_2) \ \tfrac{(x_2-\bar{x}_2)^2}{2!}\right]. \end{aligned} \tag{14}$$

Note that inserting the polynomial vector $\mathbf{p}$ into Eqs. (7) and (8) generates $\mathbf{M}$ and $\mathbf{B}$ matrices, and the derivative coefficient vector $\mathbf{a}$ can be computed as in Eq. (6). Since the derivative coefficient vector $\mathbf{a}$ includes all of the derivatives for $u(\mathbf{x})$ as described in Eq. (4), the governing partial differential equations can be directly discretized in terms of the discretized differential operators in Eq. (10). Further details about discretizing the partial differential equations within the similar context of phase field analysis can be found in the literature [28].

2.2 Multi-phase field model for non-equilibrium solidification

For the completeness, we briefly introduce the non-equilibrium solidification model derived with the diffusive interface approach; note that the non-equilibrium solidification model adopted here is based on the multi-phase field model with finite interface dissipation [8, 9]. Since the adopted model does not require an equal diffusion potential for chemical fields across solidification interface, it is suitable for predicting rapid solidification phenomena subjected to extreme temperature gradients and rates.

For the solidification of multi-component alloy system, the simplified free energy description in a computational domain $\boldsymbol{\Omega} \in \mathbb{R}^2$ is considered with the contributions from the interfacial energy f^{inf} and the chemical energy f^{chem}. The total free energy functional F of the system is written as

$$F(\boldsymbol{\phi}, c) = \int_{\Omega} (f^{\text{inf}}(\boldsymbol{\phi}) + f^{\text{chem}}(\boldsymbol{\phi}, c))\mathrm{d}\Omega \tag{15}$$

where $\boldsymbol{\phi} = (\phi_1, \ldots, \phi_\alpha) *$ and $\mathbf{c} = \left\{\left(c_1^1, \ldots, c_1^i\right), \ldots, \left(c_\alpha^1, \ldots, c_\alpha^i\right)\right\}$ denote phase field order parameters for the phase and concentration fields, respectively. For the system consisting of N phase (i.e. liquid, FCC, BCC, etc.) with n chemical components (i.e. C, Cr, Ni, etc.), $\alpha \in [1, N]$ and $i \in [1, n]$ are considered. For the subsequently described multi-phase field model, we will use Greek letter to denote phases while lower case alphabet for chemical concentrations.

The interfacial and chemical free energy density at the material point $\mathbf{x}$ is defined by

$$\begin{aligned} f^{\text{inf}} = \sum_{\alpha=1}^{N}\sum_{\beta=\alpha+1}^{N}\Bigg[& \frac{4\sigma_{\alpha\beta}}{\eta}\left(-\frac{\eta^2}{\pi^2}\nabla\phi_\alpha \cdot \nabla\phi_\beta + \phi_\alpha\phi_\beta\right) \\ & + \lambda\left(\sum_{\gamma=1}^{N}\phi_\gamma - 1\right)\Bigg], \end{aligned} \tag{16}$$

$$f_{\alpha\beta}^{\text{chem}} = \sum_{\gamma=1}^{N} \phi_\gamma f_\gamma(\mathbf{c}_\gamma) + \sum_{i=1}^{n-1} \lambda_{\alpha\beta}^{i}\left(c_{\alpha\beta}^{i} - \phi_\alpha c_\alpha^i - \phi_\beta c_\beta^i\right). \tag{17}$$

where $\sigma_{\alpha\beta}$ is the interfacial energy between phases α and β, η is the interface width which is set to a constant for all interfaces in this study, and f_γ is the bulk free energy of phase γ. Note that the last terms in Eqs. (16) and (17), i.e. $\sum_{\gamma=1}^{N} \phi_\gamma = 1$ and $c_{\alpha\beta}^i = \phi_\alpha c_\alpha^i + \phi_\beta c_\beta^i$ implies the constraint conditions which are described in terms of Lagrange multipliers, respectively.

Derivation of the rate ϕ_α occurs through the first variation of the free energy functional F:

$$\frac{\partial \phi_\alpha}{\partial t} = \frac{\delta F(\phi_\alpha)}{\delta \phi_\alpha} = \left(\nabla \frac{\partial F}{\partial \nabla \phi_\alpha} - \frac{\partial F}{\partial \phi_\alpha}\right) \tag{18}$$

The rate change of the phase field ϕ_α is then written as [8]:

$$\begin{aligned}\frac{\partial \phi_\alpha}{\partial t} &= -\frac{1}{N}\sum_{\beta=1}^{N}\left[\frac{\mu_{\alpha\beta}\pi^2}{4\eta}\left(\frac{\delta F}{\delta \phi_\alpha} - \frac{\delta F}{\delta \phi_\beta}\right)\right] \\ &= \frac{1}{N}\sum_{\beta=1}^{N}\frac{\partial \psi_{\alpha\beta}}{\partial t}\end{aligned} \tag{19}$$

where

$$\begin{aligned}\frac{\partial \psi_{\alpha\beta}}{\partial t} = K_{\alpha\beta}\Big\{\Big[&\sigma_{\alpha\beta}\left(I_\alpha - I_\beta\right) \\ &+ \sum_{\gamma=1,\gamma\neq\alpha,\gamma\neq\beta}^{N}\left(\sigma_{\beta\gamma} - \sigma_{\alpha\gamma}\right)I_\gamma\Big] + \frac{\pi^2}{4\eta}\Delta g_{\alpha\beta}\Big\}\end{aligned} \tag{20}$$

$$I_\gamma = \nabla^2 \phi_\gamma + \frac{\pi^2}{\eta^2}\phi_\gamma \tag{21}$$

$$K_{\alpha\beta} = \frac{4N\eta\left(\phi_\alpha + \phi_\beta\right)\mu_{\alpha\beta}}{4N\eta\left(\phi_\alpha + \phi_\beta\right) + \mu_{\alpha\beta}\pi^2\sum_{i=1}^{n-1}\frac{\left(c_\alpha^i - c_\beta^i\right)^2}{P_{\alpha\beta}^i}} \tag{22}$$

$$\Delta g_{\alpha\beta} = f_\beta - f_\alpha - \sum_{i=1}^{n-1}\frac{\phi_\alpha \tilde{\mu}_\alpha^i + \phi_\beta \tilde{\mu}_\beta^i}{\phi_\alpha + \phi_\beta}\left(c_\alpha^i - c_\beta^i\right) \tag{23}$$

As shown in Eq. (19) the phase field and its rate are determined by the sum total of interface fields $\frac{\partial \psi_{\alpha\beta}}{\partial t}$ for all active phase pairs ϕ_α and ϕ_β acting at each point in a region of active phase transformation, i.e. $0 > \phi_\alpha > 1$ called the *interphase region*. The evolution of each phase pair within this interfacial region as described by Eq. (20) is driven by *thermodynamic* or *chemical* source term $\Delta g_{\alpha\beta}$. Note that the driving force $\Delta g_{\alpha\beta}$ depends on by differences in temperature T and phase composition c that determine Gibbs free energy $f_\alpha(T, c_\alpha)$ and $f_\beta(T, c_\beta)$, and their derivatives $\tilde{\mu}_\alpha^i\left(=\frac{\partial f_\alpha}{\partial c_\alpha^i}\right)$ and $\tilde{\mu}_\beta^i\left(=\frac{\partial f_\beta}{\partial c_\beta^i}\right)$ with respect to the corresponding phases α and β, respectively; the computation of Gibbs free energy f can be found in Appendix A. The set of terms contained within the square bracket of Eq. (20) are dependent on the phase field surface and its curvature scaled by the interfacial energy $\sigma_{\alpha\beta}$; here, $\Delta g_{\alpha\beta}$ acts on this set and the associated response, a function of phase field geometry, determines the direction of phase change, i.e. melting or solidification. Additionally, phase evolution is scaled by a kinetic coefficient $K_{\alpha\beta}$ as shown in Eq. (22) where $\mu_{\alpha\beta}$ is the interfacial mobility at the boundary of phases α and β and $P_{\alpha\beta}$ is the interfacial permeability which plays a significant role governing the magnitude of $K_{\alpha\beta}$ and therefore, the evolution *speed* of $\dot{\psi}$. Further discussions about the implications of the adopted phase filed model, i.e. Eqs. (16)–(23) can be found in the literature [8–10].

The diffusion behavior of multi-component alloy [8] during the solidification is governed by

$$\begin{aligned}\frac{\partial c_\alpha^i}{\partial t} = \frac{1}{\phi_\alpha}\Bigg[&\nabla\cdot\left(\phi_\alpha\sum_{j=1}^{n-1}D_{ij}^{\alpha,n}\nabla c_\alpha^i\right) + \sum_{\beta=1}^{N}P_{\alpha\beta}^i\frac{\phi_\alpha\phi_\beta\left(\tilde{\mu}_\beta^i - \tilde{\mu}_\alpha^i\right)}{\phi_\alpha + \phi_\beta} \\ &+ \sum_{\beta=1}^{N}P_{\alpha\beta}^i\frac{\phi_\alpha\left(c_\beta^i - c_\alpha^i\right)}{N\left(\phi_\alpha + \phi_\beta\right)}\frac{\partial \psi_{\alpha\beta}}{\partial t}\Bigg].\end{aligned} \tag{24}$$

In the limit as $P_{\alpha\beta}^i$ approaches infinity, the classical phase-field model with equal diffusion potentials are naturally recovered. The first term within the square brackets accounts for the diffusion flux across the domain boundary where the diffusion coefficient $D_{ij}^{\alpha,n}$ provides a relationship between the components of the flux and the spatial gradient of the chemical species component $\mathbf{c}^i$ for phase α. The other two terms are only active within the region of phase transformation. Differences in phase chemical potential drive the second term and the phase field evolution itself influences the last term.

2.3 Discretized equations

For the rapid solidification analysis, Eqs. (19) and (24) are mainly required to be evaluated to predict the evolution of phase changes and the chemical concentrations of the alloy system. Discretization of continuous spatial derivatives embedded within these governing equations occurs by replacement with their discrete differential counterparts, i.e. Eq. (10) at all discrete points in the domain. The derivative quantities below are resolved along the standard basis triad. Throughout the following section, indicial and

direct notation are used interchangeably where the mth spatial component of an object, say the vector $\mathbf{x}$, is denoted by x_m . Repeated indices on a term implies summation up to the number of spatial dimensions and is set to $\mathbb{R}^2$. As described in Sect. 2.1, the continuous scalar field u is discretized into a finite set of N points u_I where I corresponds to the node number; i.e. $I \in [1, N]$. For simplicity, the discretized forms of the divergence of the gradient, or Laplacian $\nabla^2(\cdot) = \partial^2(\cdot)/\partial x_m x_m$ operator on the field on c at the point $\mathbf{x}$ defined as

$$\nabla^2 u(\mathbf{x}) = \frac{\partial^2 u(\mathbf{x})}{\partial x_m^2} = \sum_{I=1}^{N} \left[\Phi_I^{(2,0)}(\mathbf{x}) + \Phi_I^{(0,2)}(\mathbf{x})\right] u_I. \tag{25}$$

A two-field derivative product is discretized as:

$$\begin{aligned} \frac{\partial \phi}{\partial x_m}\frac{\partial c}{\partial x_m} = &\sum_{I=1}^{N} \Phi_I^{(1,0)} \phi_I \sum_{I=1}^{N} \Phi_I^{(1,0)} c_I \\ &+ \sum_{I=1}^{N} \Phi_I^{(0,1)} \phi_I \sum_{I=1}^{N} \Phi_I^{(0,1)} c_I. \end{aligned} \tag{26}$$

For particular components i, j and phase, α, the diffusion term for a species in Eq. (24) can be expanded as:

$$\begin{aligned} \nabla \cdot (\phi_\alpha D_{ij}^{\alpha,n} \nabla c_\alpha^j) &= \frac{\partial}{\partial x_m}\left(\phi_\alpha D_{ij}^{\alpha,n} \frac{\partial c_\alpha^j}{\partial x_m}\right) \\ &= D_{ij}^{\alpha,n} \frac{\partial \phi_\alpha}{\partial x_m}\frac{\partial c_\alpha^j}{\partial x_m} + \phi_\alpha \frac{\partial D_{ij}^{\alpha,n}}{\partial x_m}\frac{\partial c_\alpha^j}{\partial x_m} + \phi_\alpha D_{ij}^{\alpha,n} \frac{\partial^2 c_\alpha^j}{\partial x_m x_m} \end{aligned} \tag{27}$$

where Eqs. (25) and (26) are used to discretize each of the three terms in Eq. (27). Note that all subsequent analyses in this study set $D_{ij}^{\alpha,n}$ to a constant thereby reducing Eq. (27) to two terms. Note that for those interested, verification of the computed discrete differential operators and an analysis of the interpolation error using the Method of Manufactured solutions for a diffusion term, i.e. similar to Eq. (27) are presented in Appendix B.

3 Computational implementation

The generalized Crank–Nicolson time-stepping scheme is used for temporal integration of the phase field evolution equations; the numerical stability of the generalized Crank–Nicolson algorithm has been extensively tested within the similar contexts [28, 32, 33].

$$\frac{\varphi^{n+1} - \varphi^n}{\Delta t} = \theta \mathbf{r}^{n+1} + (1-\theta)\mathbf{r}^n \tag{28}$$

where θ ranges from 0 (forward Euler) to 1 (backward Euler), the index n represents the time step, and $\mathbf{r} \in \mathbb{R}^{[N\times 1]}$ corresponds to the collection of calculated phase field, $\dot{\phi}$, and concentration, $\dot{\boldsymbol{c}}_\alpha$, rates $\forall \mathbf{x} \in \Omega \cup \partial\Omega$ as given by Eqs. (19) and (24), respectively.

$$\mathbf{c}^{n+1} = \Delta t\left[\theta \dot{\mathbf{c}}^{n+1} + (1-\theta)\dot{\mathbf{c}}^n\right] + \mathbf{c}^n \tag{29}$$

$$\phi^{n+1} = \Delta t\left[\theta \dot{\phi}^{n+1} + (1-\theta)\dot{\phi}^n\right] + \phi^n \tag{30}$$

A forward Euler approach is used in this study.

Details to implement spatial discretization and time integration are as follows:

1. Spatial discretization: discretize Ω with desired amount of collocation points, N_{tot}, and calculate differential operators:
   (a) Define the desired discretization level consisting of N_{tot} within Ω and on its boundary $\partial\Omega$.
   (b) Define the spatial dimension, n, and desired order of differentiation, m. Both parameters must meet the differentiability and spatial requirements embedded within the governing equations. For example, $m = 2$ is the minimum to solve the classical Poisson's problem.
   (c) At each local center $\bar{\mathbf{x}} \in \Omega \cup \partial\Omega$ where at that point $\mathbf{x} = \bar{\mathbf{x}}$, define the desired amount of neighbors directly N_{nbr} or through the dilation parameter, $\rho_{\bar{\mathbf{x}}}$, which defines the radius of compact support, i.e. the neighborhood of $\bar{\mathbf{x}}$. In practice, it is often sufficient to assume a constant N_{nbr} or $\rho_{\bar{\mathbf{x}}}$ $\forall \bar{\mathbf{x}} \in \Omega \cup \partial\Omega$, although further optimization can be achieved by varying N_{nbr} or $\rho_{\bar{\mathbf{x}}}$ at each $\bar{\mathbf{x}}$.
   (d) At each point, $\mathbf{x}$, use Eqs. (7) and (8) to construct $\mathbf{M}(\mathbf{x})$ and $\mathbf{B}(\mathbf{x})$, and then generate shape functions, i.e. $\boldsymbol{\Phi}(\mathbf{x}) = \mathbf{M}^{-1}(\mathbf{x})\mathbf{B}(\mathbf{x})$. Apply the calculated shape functions $\boldsymbol{\Phi}(\mathbf{x})$ to discretize the diffusion term, i.e. Eq. (27) through Eqs. (25) and (26).
2. Temporal integration: Apply Crank–Nicholson time stepping scheme to a set of discretized equations by:
   (a) Initialize fields for each solute with respect to the solvent and phase fields within each solute.
   (b) Apply Eqs. (19)–(24) to compute rates for the phase $\dot{\phi}$ and concentration fields $\dot{c}$.
   (c) Update and repeat.

4 Numerical examples

4.1 Non-equilibrium solidification of Al–Sn binary alloy

All examples within Sect. 4 consider solidification of Al-0.2 at% Sn alloy with FCC-A1 and BCT-A5 phases present in the system. The eutectic temperature, i.e. the FCC and BCT solidification point, occurs at 502 K. Our region of interest for this study is located within the encircled region of Fig. 1a where at 860 K the FCC phase precipitates out of solution above the eutectic temperature. The FCC and liquid Gibbs free energy curves associated with this region is shown in Fig. 1b. Initial conditions for this system produces a negative difference in Gibbs energy with a value of ≈ 800 J/mol indicating a liquid to solid spontaneous transformation. Both phases are initialized to the same concentration of $c_{\text{liq}} = c_{\text{sol}} = 2.0 \times 10^{-4}$ for all points in the domain.

Thermochemical parameters and equations used to construct the Gibbs free energy curves, $\Delta\tilde{g}(c, T)$ are taken from the COST-507 [34] database. Interested readers may refer to Section A for construction and implementation details of $\Delta\tilde{g}(c, T)$ developed for this study. All input parameters are summarized in Table 1 with several sourced from other studies [10]. The solid (FCC) phase within any grain are assumed impermeable relative to one another and the diffusivity coefficient for solid phases are set to zero.

Discretization occurs over a $10 \times 10\,\mu\text{m}^2$ square domain with periodic boundary conditions applied to each of the four edges. To gain insight to the evolution equations, Eqs. (19)–(24) and terms within, we begin with a simple case of two grains symmetrically positioned along the horizontal centerline of the computational domain. A visual

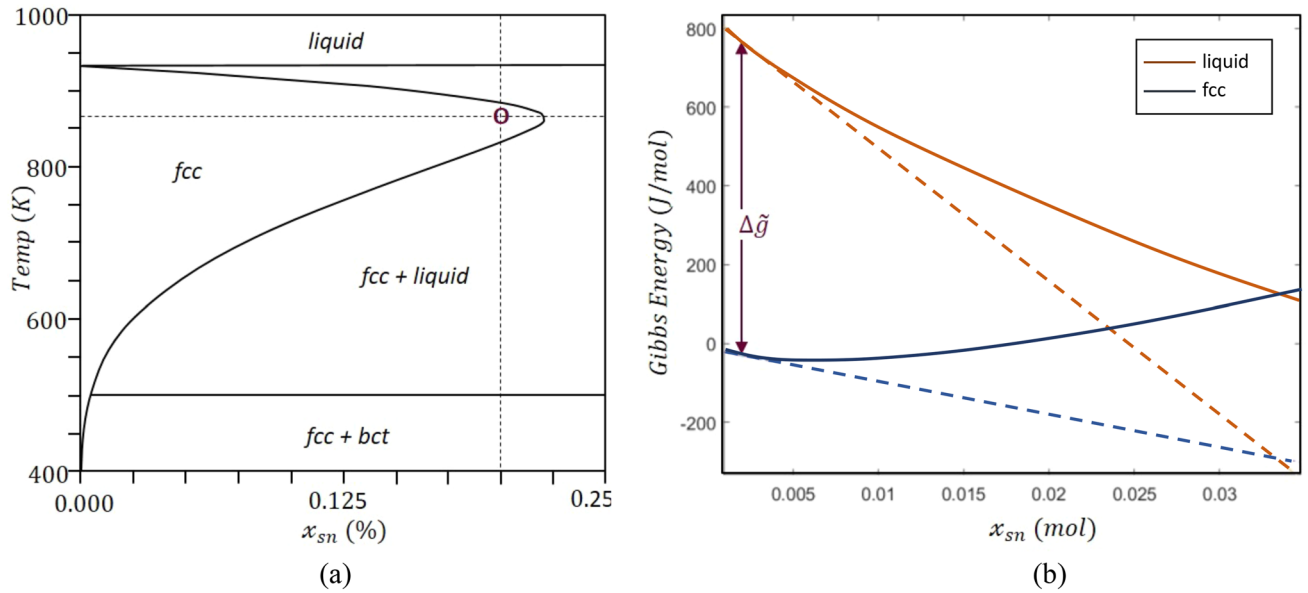

Fig. 1 An illustration of: **a** the Al–Sn phase diagram for low Sn concentrations where the encircled region corresponds to the point (0.02 at% Sn, 860 K), and **b** the corresponding Gibbs free energy curves at 860 K

Table 1 Simulation parameters for Al–Sn alloy

Nomenclature	Symbol	Value	Units	Source
Liquid diffusion coefficient	D_l	1.3×10^{-7} exp(23.8 kJ/RT)	m^2/s	[10]
Solid diffusion coefficient	D_s	0	m^2/s	[10]
Solid/liquid interface permeability	P_{ls}	1×10^{-5}	m^3/Js	[10]
Solid/solid interface permeability	P_{ss}	0	m^3/Js	–
Solid/liquid interface mobility	M_{ls}	5×10^{-8}	m^4/Js	[10]
Solid/solid interface mobility	M_{ss}	0	m^4/Js	–
Time step	Δt	1×10^{-10}	s	–
Domain length	L	10	μm	–
Molar volume	v_m	10	cm^3/mol	–

rendering of the discretized system with two grains at the early stages of growth is shown in Fig. 2.

In this case, there exist three phase fields $\alpha \in \{1, 2, 3\}$ where 1 = liquid, 2 = grain$_1$, and 3 = grain$_2$ and each phase field is endowed with its own independent concentration, c_α, field. The concentration of Sn in Al, i.e. c^{Sn} at any point [9] is then given by:

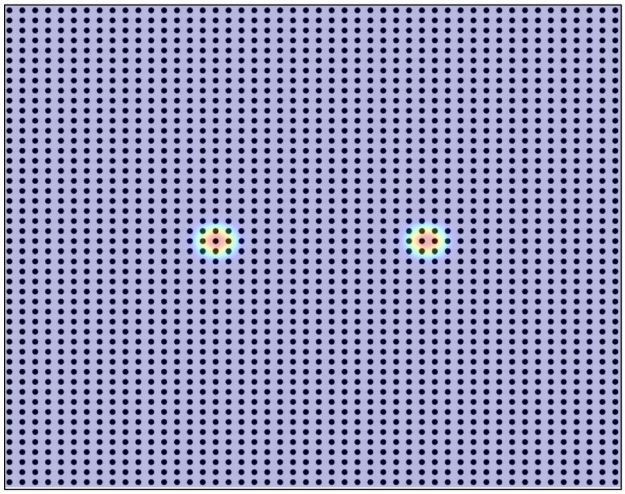

Fig. 2 A schematic of the computational domain with 2500 collocation points (black dots) for the Al-0.2 at% Sn alloy from the perspective of the solid phase field where order parameter values correspond to 1 for red and 0 for blue

$$c^{\mathrm{Sn}} = \sum_{\alpha=1}^{3} \phi_\alpha^{\mathrm{Sn}} c_\alpha^{\mathrm{Sn}} \tag{31}$$

along with the constraint condition

$$\sum_{\alpha=1}^{3} \phi_\alpha^{\mathrm{Sn}} = 1. \tag{32}$$

To examine each of the terms in Eq. (20), it is helpful to perform a visual dissection of the rate equation. This is shown in Fig. 3, which consist of a snapshot of the phase field profile at the 100th step in the simulation with corresponding section values along the centerline at $\mathbf{x} = (0, L/2)$. The centerline values in Fig. 3b represent the terms embedded within Eq. (20). These energy terms, one of geometry and the other chemical are generally of opposite sign and in this case, the chemical energy clearly dominates in magnitude. This results in a positive sum as shown with the dashed line in Fig. 3b, thereby driving the material towards solidification. The sum is scaled by the kinetic coefficient as described by Eq. (22) to produce the phase field rate shown in Fig. 3c, which over an increment of time, yields changes to the phase field geometry. The changing phase field geometry evolves into a shape that tends to temper or resist the chemical driving force. This is evident by observation of the inflections points located near the outer edges of the active interphase region, i.e. $0 < \phi_\alpha < 1$. The set of phase field values bounded within the inflection points are negative in curvature and of larger magnitude relative to the other points , the combination of these values is the capillary term given by Eq. (21).

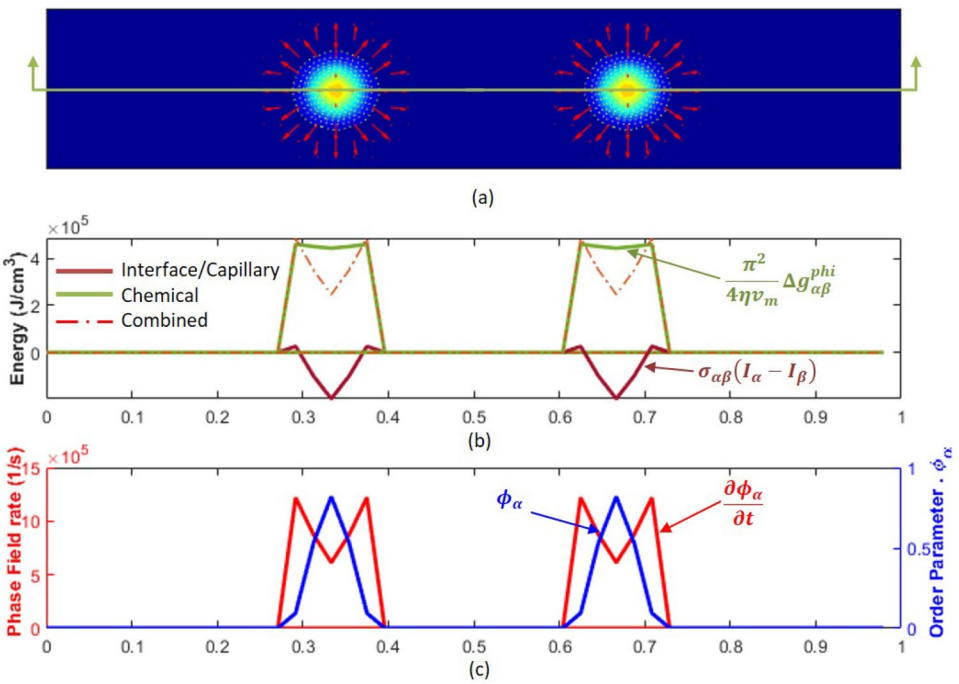

Fig. 3 A snapshot of the phase field in the regions of active interphase conditions where: **a** the red arrows correspond to the negative gradient of the chemical potential driving the phase field outward, **b**, **c** centerline values along for the various terms within the phase field evolution equation

Temperature is only independent parameter external to the system and it along with the phase composition, feed the chemical potential and its force gradient.

We now move to the concentration field where per Eq. (31), sum of phase weighted components $\phi_\alpha c_\alpha$ determines the overall concentration field c^{Sn}. Therefore, it is of interest to understand the effect of $\phi_\alpha c_\alpha$ on the evolution of c^{Sn}. Our analysis begins with the concentration fields displayed in Fig. 4 at six instances in time detailing the overall concentration field and its phase weighted components. For reference a phase field surface plot is also embedded within each frame. Recall, that the phase weighted concentration profiles are initialized to 0.02 at% Sn. Regions of active phase transformation are bounded with the dashed lines of the cross-sectional plots. Evolution begins with a liquid to solid transition about the initial seed locations, Fig. 4a, b, eventually leading to small region that is fully solidified Fig. 4c, and finally radial growth Fig. 4d–f. Only the diffusion term, i.e. the first term in Eq. (24) affects the concentration rate for points outside of the interphase region where for this set of points $c^{\mathrm{Sn}}_{\mathrm{liq}} = \phi_{\mathrm{liq}} c_{\mathrm{liq}}$ and $c^{\mathrm{Sn}}_{\mathrm{sol}} = \phi_{\mathrm{sol}} c_{\mathrm{sol}}$ are constant. Concentration values for points located close to the outer edge but still within the interphase or transition region undergo an initial reduction due to the influence of $c^{\mathrm{Sn}}_{\mathrm{liq}}$. After some time, $c^{\mathrm{Sn}}_{\mathrm{sol}}$ eventually dominates and guides c^{Sn} into its final state.

The computational requirements needed to conduct the simulations for this study are categorized into two stages; the time required to calculate differential operators, and the time required to numerically integrate and update the evolution equations (Eqs. 19–24). Both categories are shown in Table 2 for three discretization levels up to the point of interphase contact; see Fig. 5. Calculation of differential operators need only occur once for a given discretization and the relationship to discretization level is linear. The

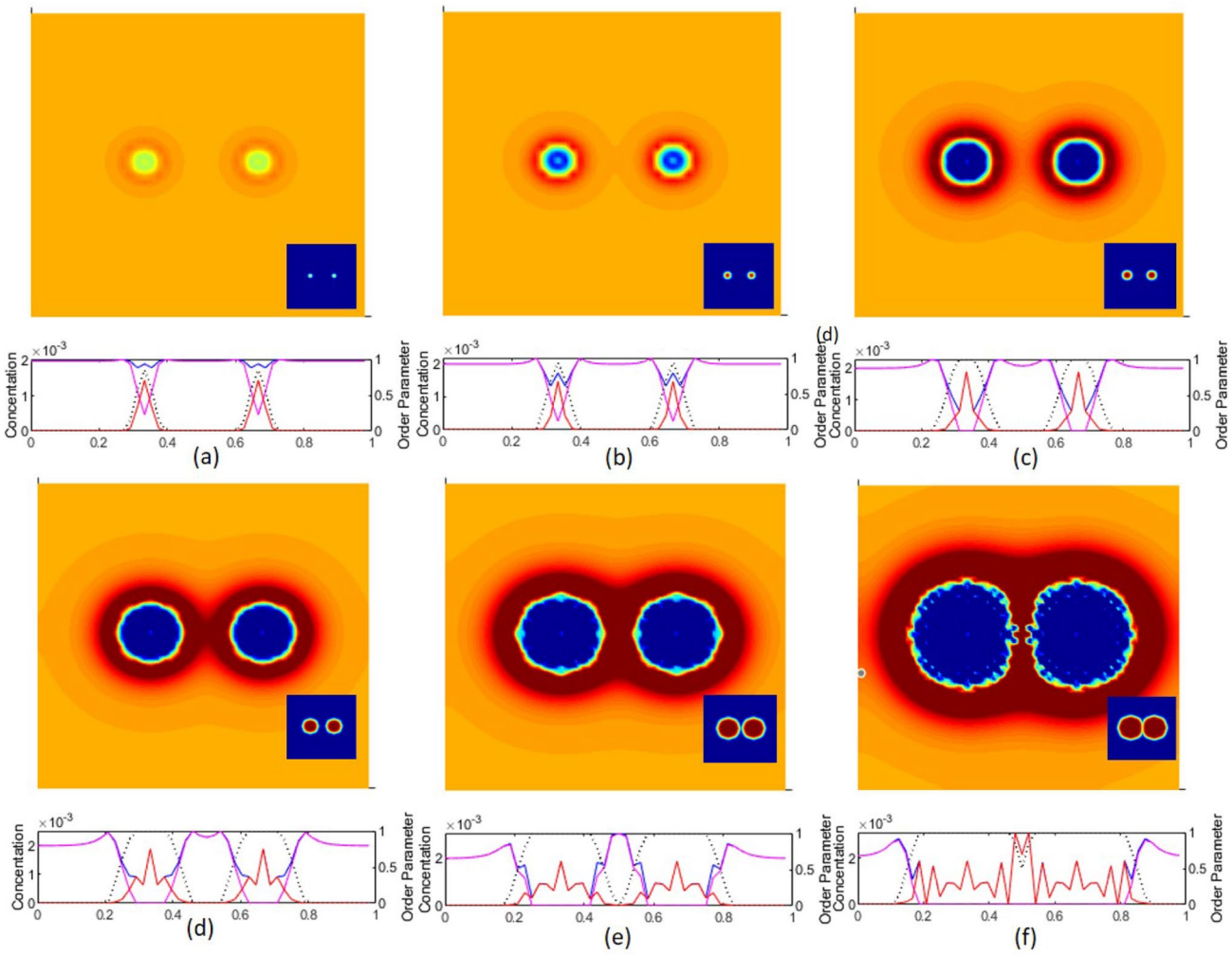

Fig. 4 Contour plots of the overall concentration where the line plots below each contour plot represent field values for overall concentration c^{Sn}, its solid component $\phi_{\mathrm{sol}} c_{\mathrm{sol}}$, and liquid component $\phi_{\mathrm{liq}} c_{\mathrm{liq}}$ are displayed in blue, red and magenta, respectively

Table 2 A comparison of required times to construct differential operators, and simulate evolution of two grains for three discretization levels

# points	Computational costs (s)		
	Differential operators	Grain simulation	Total
2500	22.8	41.8	64.6
3600	33.2	87.8	121.0
4900	45.7	221.9	267.6

computational requirements for temporal integration, however, appear to exhibit quadratic rate. This is attributed to the fact that finer discretizations produce more points within the interphase region.

Now consider the case of 10 grains with the same material properties as given in Table 1. Recognize that each grain is *assigned* a phase where inter-grain permeabilities and mobilities between solid/grain phases are set to zero. Ten seeds are randomly distributed throughout the domain with a uniform initialization of all concentration fields c_α at a value of 0.02 at% Sn in Al. Fig. 6 is a collection of concentration and phase values observed at six instances of time. The liquid phase concentration component $\phi_{\text{liq}} c_{\text{liq}}$ initially dominates the overall field behavior Fig. 6a. At this stage, Sn particles begin to evacuate out of the solidifying material resulting in an elevated concentration profile extending from the outer rim of the interphase region into the liquid. Driven by its gradient, the elevated concentration fields then radiate out towards and eventually join one another Fig. 6b, c. Solid–solid interphase evolution is suppressed in active regions involving two or more grains. This is attributed to the impermeability condition which drives the kinetic coefficient $K_{\alpha\beta}$ to zero. Grain growth partitions the liquid into distinct areas, each enclosed by an intergrain boundary, resulting in an overall increase in concentration within these areas Fig. 6d. and continues until the domain is fully solidified Fig. 6e. As shown in Fig. 6o, higher concentrations of Sn in the fully solidified material occur at the grain boundaries with the highest levels located at intergrain regions consisting of four or more adjacent grains.

4.2 Epitaxial growth

Some manufacturing and joining processes including additive manufacturing and welding involve solidifying a liquid metal over a solid substrate [3]. The solid substrate serves as a site for epitaxial nucleation whereby newly formed crystals nucleate at the adjacent substrate grains. Furthermore, the crystal's crystallographic orientation does not change throughout the process. The resulting morphologies, a function of the liquid temperature gradient and solidification rate, are categorized by solidification modes to include planar, cellular, dendritic, and columnar [35].

A computational domain Ω partitioned into lower Ω^1 and upper Ω^2 parts as shown in Fig. 7 is used to simulate this process in two stages; substrate synthesis followed by epitaxial growth. Substrate synthesis begins with a random distribution of seeds in Ω^1 from which crystals nucleate and grow as described by Eqs. (19)–(24). This process continues until $\phi_{\text{liq}} = 0$ for all points in Ω^1. The substrate concentration and phase fields in Ω^1 then serve as initial/boundary values for Ω^2.

Thermodynamic inputs for this study data are taken from the previous analysis, refer to Fig. 1 and Table 1 for details. Ω is set to a size of $10 \times 20\,\mu\text{m}^2$ and discretized with 5000 collocation points. Substrate synthesis begins by initializing Ω^1 with 20 randomly distributed seed sites. As shown Fig. 8, liquid to solid phase transformation continues resulting into a fully solidified multi-grain structure during which time, Al and Sn distributions tend to concentrate towards grain centers and grain boundaries respectively. The resulting Ω^1 field values are then inserted into the lower half Ω and serve as seed sites for solidification in Ω^2. The resulting morphology exhibits a planar type mode consisting of three large grains extending from the substrate surface. However, it should be stressed that the formation of smaller sub-grain during the solidification process can be either numerical artifact or physical behavior (Fig. 9).

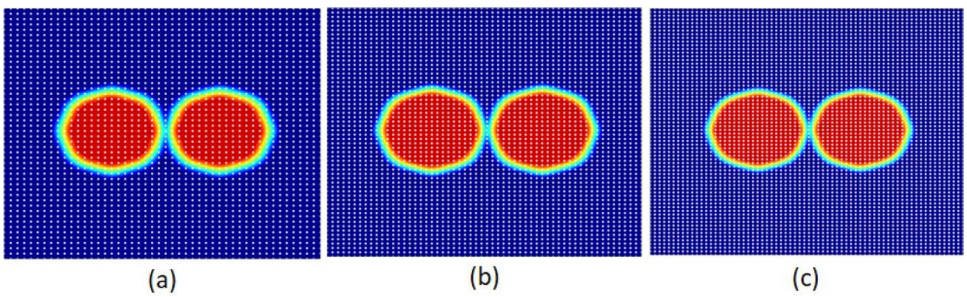

Fig. 5 Phase field contours corresponding the simulation times in listed in Table 2 for: **a** 2500, **b** 3600, and **c** 4900 collocation points

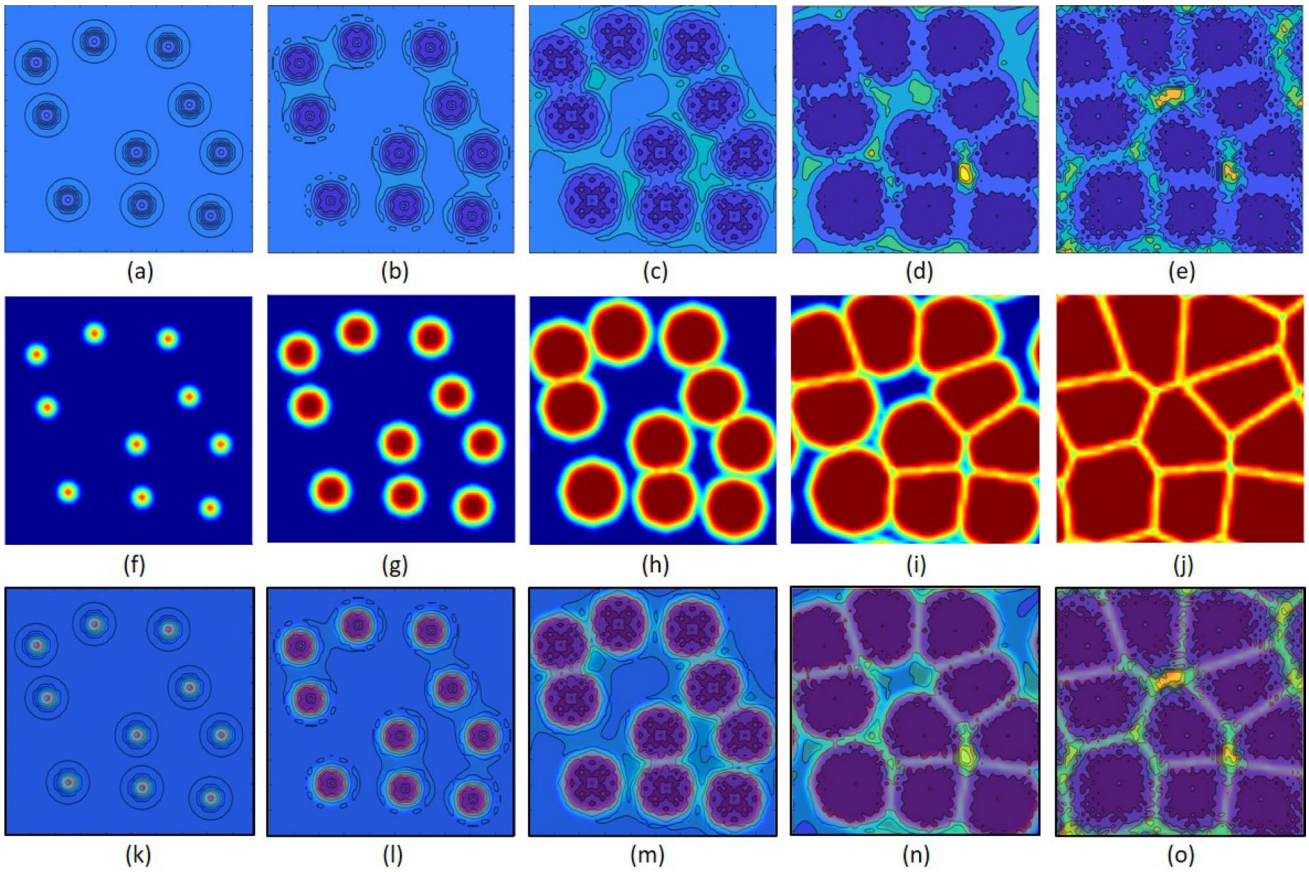

Fig. 6 Contour plots of: **a**–**e** the overall concentration field for ten grains at various instances in time, **f**–**j** corresponding phase fields, and **k**–**o** the phase image superimposed on top of the overall concentration field

5 Conclusions

A strong form-based collocation methods has been applied to discretize a multi-phase field model developed by [8] and study non-equilibrium, i.e. rapid solidification behavior for an Al-0.2 at% Sn alloy with the finite dissipation effects. Temperatures for the dilute alloy were set between liquid and eutectic regions, at a point where the solid Al, i.e. FCC phase evolves from the mixture. Gibbs energy curves for the system were constructed from experimental parameters and methodologies given in the COST-507database [34]; note that details are described in Appendix A.

Initial analysis of two symmetrically positioned grains under periodic boundary conditions illustrated interface and chemical free energy effects on phase and concentration field kinetics. Subsequent multi-grain solidification studies for the 10-grain and 20-grain case provided insight in the concentration profile of the fully solidified material. The results show that solid phase Al forming within grain interior with Sn solute ejected towards the boundary with highest concentrations located the intersection of multiple grain boundaries. Finally, the field equations were evaluated for alloy solidification in the presence of a 20-grain substrate. A resulting morphology exhibited a planer type solidification mode with three large grains extending from the grains substrate surface. A smaller subgrain can be either a physical or numerical artifact, formed during solidification, and current research is underway to determine the cause.

Future works following this study include expanding the existing framework to evaluate a binary solution in $\mathbb{R}^3$, and evaluation of ternary solution in $\mathbb{R}^2$ and in $\mathbb{R}^3$. Another interesting future work will be evaluating the influence of initial stress on the solidification process by minimizing the total elastic strain energy under an applied elastic strain toward the orientation-dependent growth of grains [2, 21, 36].

Appendix 1: Implementation of the Gibbs free energy

The bulk (Gibbs) free energy f_γ for phase γ evaluated in this work are based on the experimental thermo-chemical data and methods provided within the COST-507 [34]. Data consists of a collection of coefficients and interaction parameters

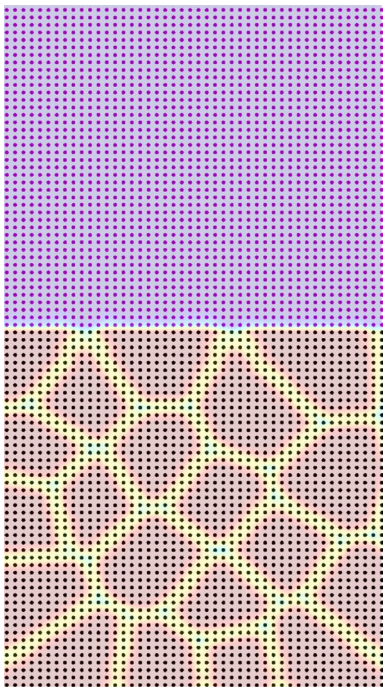

Fig. 7 Discretized $10 \times 20\,\mu m^2$ computational domain of Al-0.2% Sn mixture formed by a union of solid domain, i.e. lower half and liquid domain, i.e. upper half

used to calculate free energies of pure element and multi-component systems. The coefficients are temperature T dependent and are used with the power series to evaluate the molar free energy g for a pure species i in phase γ with respect to its stable state enthalpy; i.e.

$$g_i^{\gamma}(T) - h_i^{\gamma}(298.1K) = a + bT + cT\ln T + dT^2 + eT^3 + fT^{-1} + gT^7 + hT^{-9}. \tag{33}$$

The free energy of multi-component system consists of contributions from each constituent species within the mixture and of mixing between species. Contributions from mixing are further classified as either ideal or non-ideal where the latter is modeled with a Redlich-Kister polynomial that contains temperature dependent interaction parameters L^{ν}. For a substitutional three-component alloy system, the free energy is given by

$$G^{\gamma}(x_i, T) = \sum_{i=1}^{3} x_i g_i^{\gamma} + RT \sum_{i=3}^{3} \sum_{j>i}^{3} x_i x_j \sum_{\nu=0}^{3} L_{ij}^{\nu}(x_i - x_j)^{\nu} + \sum_{i=1}^{3} \sum_{j>i}^{3} \sum_{k>j}^{3} x_i x_j x_k (x_i L_{ijk}^{0} + x_j L_{ijk}^{1} + x_k L_{ijk}^{2}) \tag{34}$$

where the right hand side terms respectively correspond to the unmixed, ideal mixing, binary non-ideal, and ternary

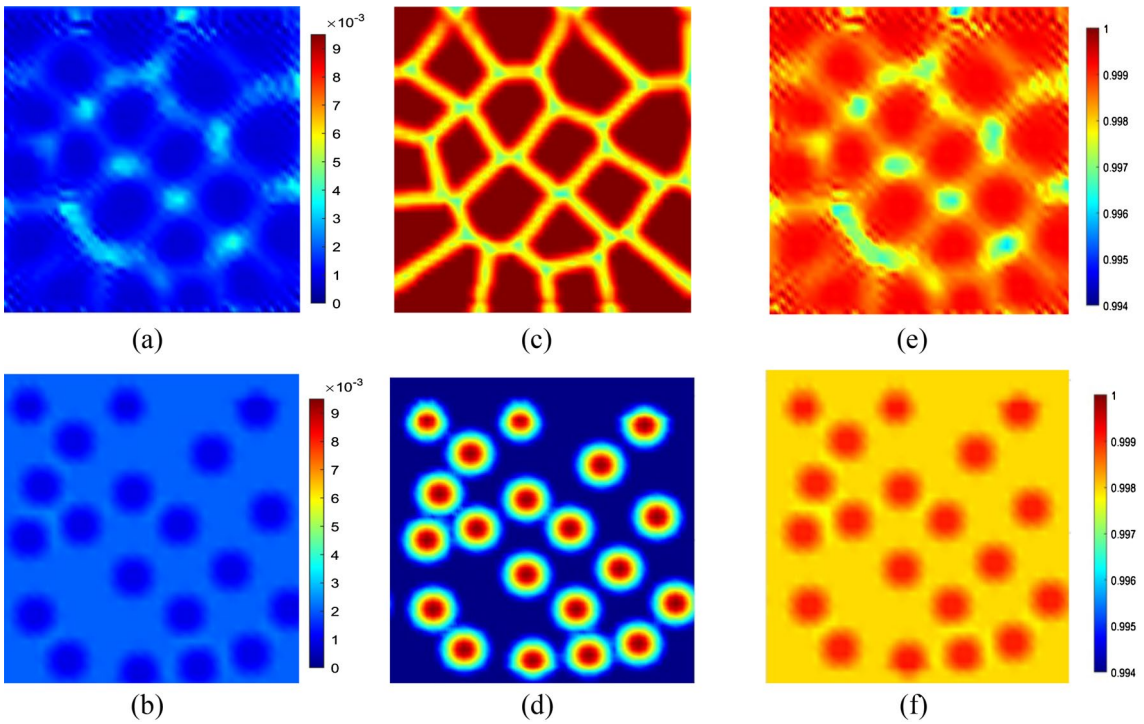

Fig. 8 Concentration and phase fields in Ω^1 for: **a** initial and **b** final Sn concentration, **c**, **d** solid phase, and **e**, **f** Al concentration

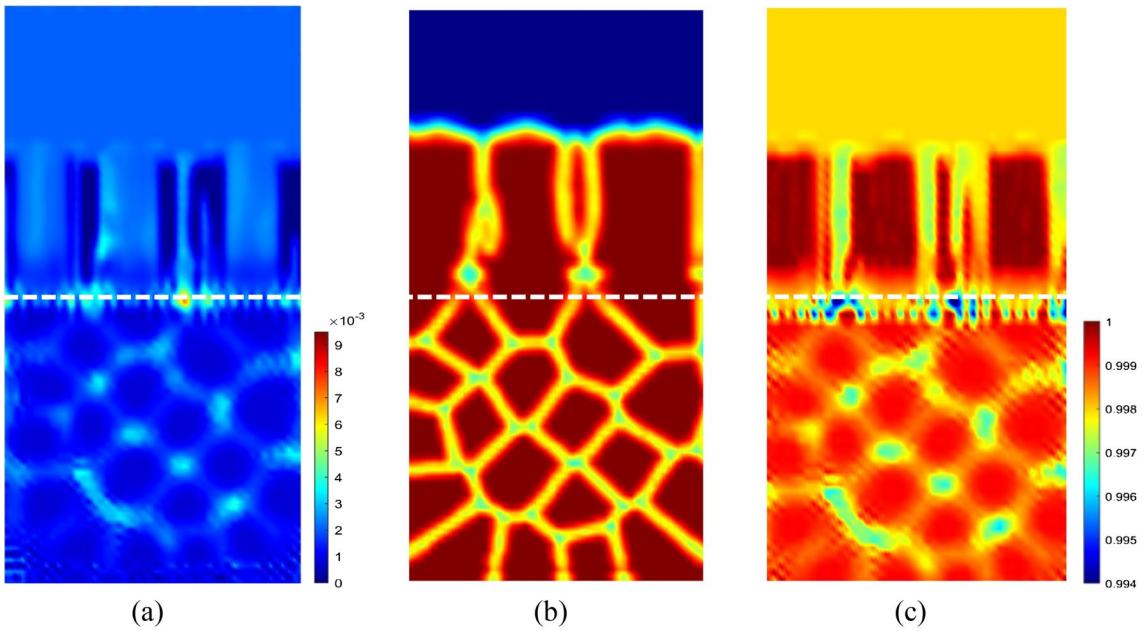

Fig. 9 Concentration and phase fields in Ω^2 for: **a** Sn concentration (upper half), **b** solid phase, and **c** Al concentration with the presence of solid substrate in Ω^1 (lower half)

non-ideal mixing terms. Invoking the chain rule to differentiate Eq. (34) with respect to composition yields

$$\frac{\partial G^{\gamma}(x_i,T)}{\partial x_m} = \frac{\partial G^{\gamma}(x_i,T)}{\partial x_i}\frac{\partial x_i}{\partial x_m} = G^{\gamma}_{,i}x_{i,m} \tag{35}$$

with

$$\begin{aligned}\frac{\partial G^{\gamma}(x_i,T)}{\partial x_m} &= \sum_{i=1}^{3} x_{i,m}g_i^{\gamma} + RT\sum_{i=1}^{3}(x_{i,m}(\ln x_i + 1)) \\ &+ \sum_{i=1}^{3}\sum_{j>i}^{3}(x_{i,m}x_j + x_{j,m}x_i) + \sum_{\nu=0}^{n} L_{ij}^{\nu}(x_i - x_j)^{\nu} \\ &+ \sum_{i=1}^{3}\sum_{j>i}^{3} x_i x_j \sum_{\nu=0}^{n} \nu L_{ij}^{\nu}(x_i - x_j)^{\nu-1}(x_{i,m} - x_{j,m}) \\ &+ \sum_{i=1}^{3}\sum_{j>i}^{3}\sum_{k>j}^{3}(x_{i,m}x_jx_k + x_ix_{j,m}x_k + x_ix_jx_{k,m})(x_iL_{ijk}^0 \\ &+ x_jL_{ijk}^1 + x_kL_{ijk}^2) \\ &+ \sum_{i=1}^{3}\sum_{j>i}^{3}\sum_{k>j}^{3} x_ix_jx_k(x_{i.m}L_{ijk}^0 + x_{j,m}L_{ijk}^1 + x_{k,m}L_{ijk}^2).\end{aligned} \tag{36}$$

Note that for the constraint, i.e. $\sum x_i = 1$ we use the conditional relation to implement Eq. (36) in our computational analysis program:

$$x_{i,m} = \begin{cases} 1 & i = m \\ -1 & i \neq m \end{cases} \tag{37}$$

Figure 10 represents an output of the Al–Sn–Zn system along the Al–Zn, Zn–Sn, and Al–Sn surfaces for the liquid, FCC, BCT and HCP phases at a temperature of 600 K. Thermo-Calc plots are also presented for comparison. The derivatives used to construct the tangent lines for the Al–Zn (lower left plot) at $x_{\mathrm{Al}} = 0.2$ are based on Eq. (36).

Appendix 2: Verification of the discrete differential operators

One way to measure the validity of computed discretized differential operators is through its fundamental properties, i.e. consistency [37]. Let x_i where $x_1 = x$ and $x_2 = y$, and to ease notation let $\Phi_I^{x_i} = \{\Phi_I^{(1,0)}, \Phi_I^{(1,0)}\}$ and $\Phi_I^{x_ix_j} = \{\Phi_I^{(2,0)}, \Phi_I^{(1,1)}, \Phi_I^{(0,2)}\}$ represent the first and second order differential operator sets respectively. For any point $p \in \bar{\Omega}$ such that $0 < p \leq N$ with associated coordinate x_i^p following properties have been numerically verified:

1. $\sum_{I=1}^{N} \Phi_I^{(0,0)} = 1$,
2. $\sum_{I=1}^{N} \Phi(\mathbf{x}^p)_I^{(0,0)}[x_i]_I = x_i$,
3. $\sum_{I=1}^{N} \Phi(\mathbf{x}^p)_I^{x_j}[x_i]_I = \delta_{ij}$,
4. $\sum_{I=1}^{N} \Phi(\mathbf{x}^p)_I^{x_ix_j}[x_ix_j]_I = 1 \quad \text{if } i \neq j$,
5. $\sum_{I=1}^{N} \Phi(\mathbf{x}^p)_I^{x_ix_j}[x_ix_j]_I = 2 \quad \text{if } i = j$.

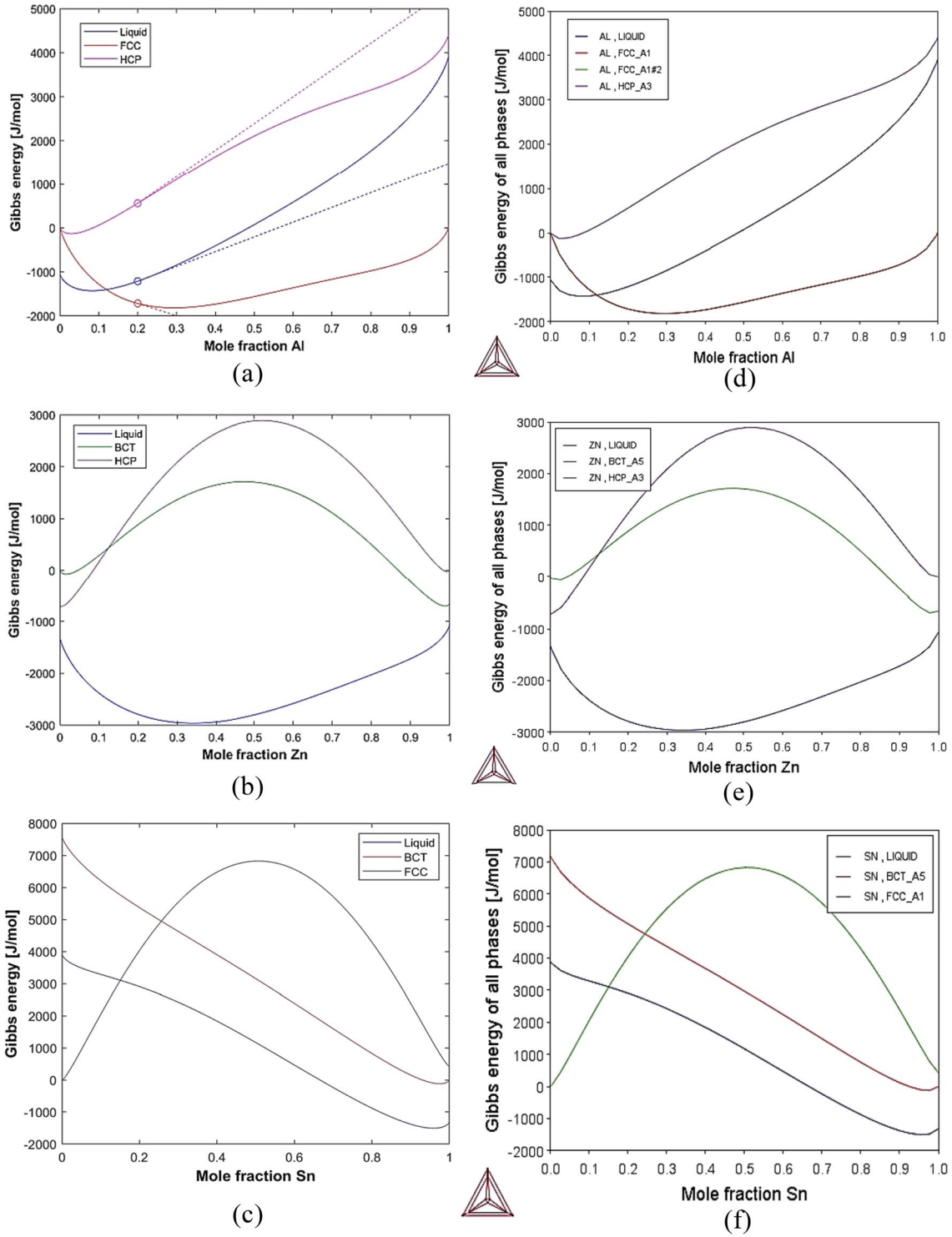

Fig. 10 Comparisons of the computed Gibbs energy (**a**–**c**) against Thermo-Calc software (**d**–**f**) at the same temperature, i.e. $T = 600$ K; the calculated Gibbs energy at along each edge of the Al–Sn–Zn ternary system, i.e. (Al, Sn, Zn = 0), (Al, Sn = 0, Zn) and (Al = 0, Sn, Zn) are shown

Note that there also exist similar properties for $\mathbb{R}^3$ domains and higher ordered derivatives (i.e $m > 2$) as well.

Another way to measure the effectiveness of differential operators is through its interpolation error. This may be achieved by benchmarking solution data for a given partial differential equation against data from another known or trusted solution analytical, numerical, or manufactured solution. In this work, we take the latter approach by

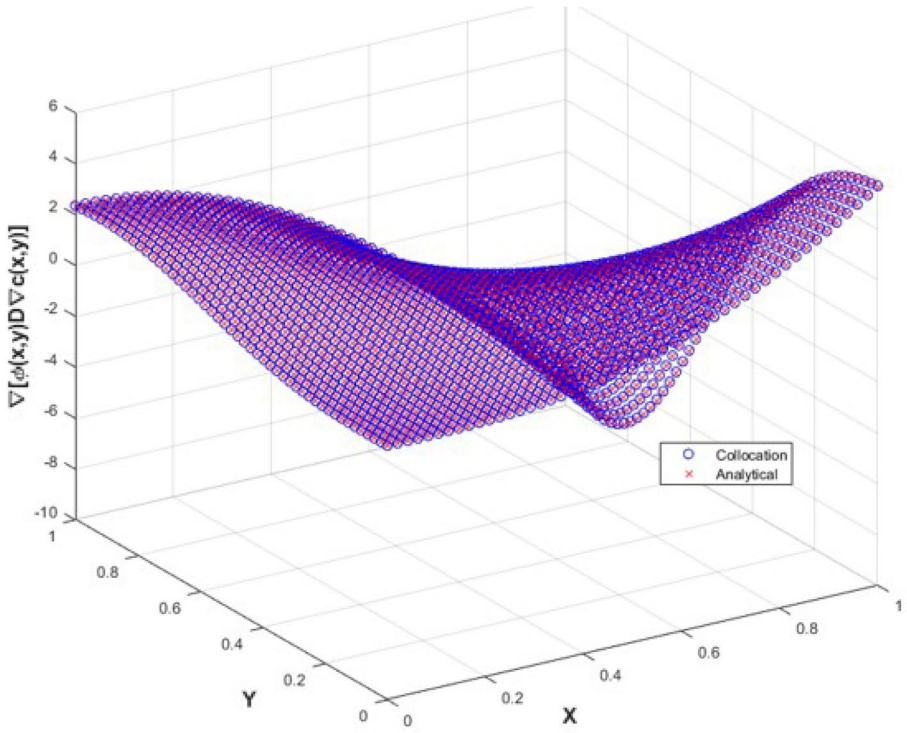

Fig. 11 Comparison of the solution surface for $\nabla \cdot (\phi(x, y)\nabla c(x, y))$; the analytical solution surface is derived based on the manufactured fields $\phi(x, y)$ and $c(x, y)$

manufacturing and differentiating two primary fields $c(x, y)$ and $\phi(x, y)$ as shown in Eqs. (38) and (39) respectively to produce a term $\nabla \cdot (\phi(x, y)\nabla c(x, y))$. The manufactured fields are variants of those taken from a helpful report on the method of manufactured solutions [38].

$$c(x, y) = c_0 \left[1 + \sin^2\left(\frac{x}{R}\right) \sin^2\left(\frac{2y}{R}\right)\right] \tag{38}$$

$$\phi(x, y) = \phi_0 \left[\frac{\sqrt{x^2 + 2y^2}}{R}\right] \tag{39}$$

Figure 11 presents a comparison between analytical y and approximate solution y^h fields for the term $\nabla(\phi(x, y)D\nabla c(x, y)$ which test all two-field first order derivative products, second order derivatives and combinations thereof; for the computation, an unit square domain is discretized with uniformly distributed 4900 collocation points. The computed discrete L_2 norm error which is given by

$$\text{error}_{L_2} = \sqrt{\left(\frac{y - y^h}{y}\right)^2} \tag{40}$$

was measured at a value less than 0.3%. Those who interested in the computational resources to construct differential operators are referred to Sect. 4 of this study.

Acknowledgements The second and third authors acknowledge support for this work by the Office of Naval Research (ONR) through the Naval Research Laboratory's core funding, and the second author also acknowledges the financial support of the Office of Naval Research under the Agile ICME Toolkit project (N0001420WX00405).

References

1. Minkoff I (1992) Solidification/liquid state processes. Springer, Berlin, pp 1–31
2. Shahnooshi E, Jamshidian M, Jafari M, Ziaei-Rad S, Rabczuk T (2019) Phase field modeling of stressed grain growth: effect of inclination and misorientation dependence of grain boundary energy. J Cryst Growth 518:18–29
3. Michopoulos J, Iliopoulos A, Steuben J, Birnbaum A, Apetre N, Song J-H, Yao F, Achuthan A, Saunders R, Bagchi A, Fonda R, Rowenhorst D, Olig S, Martin F, Moran J, Ntiros A (2021) Multiphysics integrated computational materials engineering linking additive manufacturing process parameters with part performance. In: Advances in computers and information in engineering research, volume 2. ASME, 06 (ISBN 9780791862025)
4. Aziz MJ, Smith PM (1994) Solute trapping in aluminum alloys. Acta Metall Mater 42(10):3515–3525
5. Aziz MJ, Boettinger WJ (1994) On the transition from short-range diffusion-limited to collision-limited growth in alloy solidification. Acta Metall Mater 42(2):527–537
6. Otooni MA (1998) Elements of rapid solidification: fundamentals and applications. Springer, Berlin
7. Buchmann M, Rettenmayr M (2007) Rapid solidification theory revisited—a consistent model based on a sharp interface. Scripta Mater 57(2):169–172

8. Steinbach I, Zhang L, Plapp M (2012) Phase-field model with finite interface dissipation. Acta Mater 60(6–7):2689–2701
9. Zhang ISL (2012) Phase-field model with finite interface dissipation: extension to multi-component multi-phase alloys. Acta Mater 60(6):2702–2710
10. Reuther K, Hubig S, Steinbach I, Rettenmayr M (2019) Solute trapping in non-equilibrium solidification: a comparative model study. Materialia 6:100256
11. Langer JS (1986) Models of pattern formation in first-order phase transitions. Directions in condensed matter physics: memorial in Honor of Shang-Keng Ma, vol in. World Scientific, Singapore, pp 165–186
12. Caginalp G (1989) Stefan and hele-shaw type models as asymptotic limits of the phase-field equations. Phys Rev A 39(11):5887
13. Kobayashi R (1993) Modeling and numerical simulations of dendritic crystal growth. Phys D 63(3–4):410–423
14. Wheeler AA, Boettinger WJ, McFadden GB (1992) Phase-field model for isothermal phase transitions in binary alloys. Phys Rev A 45(10):7424
15. Wheeler AA, Boettinger WJ, McFadden GB (1993) Phase-field model of solute trapping during solidification. Phys Rev E 47(3):1893
16. Boettinger WJ, Wheeler AA, Murray BT, McFadden GB (1994) Prediction of solute trapping at high solidification rates using a diffuse interface phase-field theory of alloy solidification. Mater Sci Eng A 178(1–2):217–223
17. Karma A (1994) Phase-field model of eutectic growth. Phys Rev E 49(3):2245
18. Elder KR, Gunton JD, Grant M (1996) Nonisothermal eutectic crystallization. Phys Rev E 54(6):6476
19. WheelerAdam A, McFadden GB, Boettinger WJ (1996) Phase-field model for solidification of a eutectic alloy. Proc R Soc Lond Ser A Math Phys Eng Sci 452(1946):495–525
20. Warren James A, Boettinger William J (1995) Prediction of dendritic growth and microsegregation patterns in a binary alloy using the phase-field method. Acta Metall Mater 43(2):689–703
21. Jamshidian M, Thamburaja P, Rabczuk T (2016) A multiscale coupled finite-element and phase-field framework to modeling stressed grain growth in polycrystalline thin films. J Comput Phys 327:779–798
22. Yoon Y-C, Song J-H (2014a) Extended particle difference method for weak and strong discontinuity problems: part. I. Derivation of the extended particle derivative approximation for the representation of weak and strong discontinuities. Comput Mech 53(6):1087–1103
23. Yoon Y-C, Song J-H (2014b) Extended particle difference method for weak and strong discontinuity problems: part II. Formulations and applications for various interfacial singularity problems. Comput Mech 53(6):1105–1128
24. Yoon Y-C, Song J-H (2014c) Extended particle difference method for moving boundary problems. Comput Mech 54(3):723–743
25. Yoon Y-C, Song J-H (2021) Interface immersed particle difference method for weak discontinuity in elliptic boundary value problems. Comput Methods Appl Mech Eng 375:113650
26. Almasi A, Kim T-Y, Laursen TA, Song J-H (2019a) A strong form meshfree collocation method for frictional contact on a rigid obstacle. Comput Methods Appl Mech Eng 357:112597
27. Song J-H, Yao F, Kim T-Y, Yoon Y-C, Michopoulos JG, Rabczuk T (2018) Phase field simulations of coupled microstructure solidification problems via the strong form particle difference method. Int J Mech Mater Des 14(4):491–509
28. Almasi A, Beel A, Kim T-Y, Michopoulos JG, Song J-H (2019b) Strong-form collocation method for solidification and mechanical analysis of polycrystalline materials. J Eng Mech 145(10):04019082
29. Yoon Y-C, Schaefferkoetter P, Rabczuk T, Song J-H (2019) New strong formulation for material nonlinear problems based on the particle difference method. Eng Anal Bound Elem 98:310–327
30. Beel A, Kim T-Y, Jiang W, Song J-H (2019) Strong form-based meshfree collocation method for wind-driven ocean circulation. Comput Methods Appl Mech Eng 351:404–421
31. Almasi A, Kim T-Y, Laursen TA, Song J-H (2019c) A strong form meshfree collocation method for frictional contact on a rigid obstacle. Comput Methods Appl Mech Eng 357:112597
32. Yang X, Han D (2017) Linearly first-and second-order, unconditionally energy stable schemes for the phase field crystal model. J Comput Phys 330:1116–1134
33. Thomas JW (2013) Numerical partial differential equations: finite difference methods, vol 22. Springer, Berlin
34. Saundersc N (1998) Cost 507: thermochemical database for light metal alloys. European Commission, Brussels, pp 23–27
35. Lippold JC (2015) Welding metallurgy and weldability. Wiley, New York
36. Jamshidian M, Rabczuk T (2014) Phase field modelling of stressed grain growth: analytical study and the effect of microstructural length scale. J Comput Phys 261:23–35
37. Liu W-K, Li S, Belytschko T (1997) Moving least-square reproducing kernel methods (i) methodology and convergence. Comput Methods Appl Mech Eng 143(1–2):113–154
38. Salari K, Knupp P (2000) Code verification by the method of manufactured solutions. Sandia National Labs., Albuquerque, NM, USA, Technical report